An Approach to Convert 4D Geometry into a 4D CT Scan

Pierre-Frédéric Villard, Michaël Beuve, Behzad Shariat

An Approach to Convert 4D Geometry into a 4D CT Scan

P.F. VILLARD M. BEUVE B. SHARIAT
L.I.R.I.S : Lyon Research Center for Images and Intelligent Information Systems
Bâtiment Nautibus, 8 boulevard Niels Bohr
69622 Villeurbanne Cedex, FRANCE
pierre-frederic.villard@liris.cnrs.fr

ABSTRACT

We present here an approach to convert the geometrical information produced by a physical simulation of soft-organ motion into a 3D+time CT scan. The paper describes how we calculate matter density at mesh points and how we produce dynamic 3D CT scan using the convolution parameters of medical scanners. The aim of this work is to provide physicians with standard images useful to appreciate organ motions and to incorporate them into a treatment planning platform.

Keywords

Radiotherapy, Hadrontherapy, CT Scan, Organ Motion, Simulation, Convolution, mesh, interpolation functions.

1 INTRODUCTION

A crucial problem in radiotherapy and hadrontherapy stems from organs motion due, in the case of lung tumours, to patient's breathing. Moving tumours are indeed hard to be well targeted. An improvement can be achieved with 4D CT scan providing necessary information on organs displacements.

In our latter works, we developed a pulmonary motion simulation using the well-known continuous mechanics techniques. Results consist of a "time-dependent" mesh of bulk and surface, describing various geometrical states of lung inflating [VBS+05]. We propose now to convert the displacement information into CT-scan images because of three reasons. First, we need to compare our model simulated image with real clinical CT-scan images. Second, physicians are used to proceeding only with CT scan images. Last, 4D CT scans, i.e. time varying densitometric data matrix, are to be used in a treatment planning software for dosimetry calculation. In our approach, the only inputs we need are one initial CT scan and the displacement at mesh nodes for a series of organ-motion stage. A state of the art describing the CT scan technology as well as image reconstruction techniques is presented in §2. We learn in particular that to transform motion information into CT scan two problems should to be considered: 1-Since CT scan data, namely the Hounsfield units, are obtained from the matter density, we shall see in §3 how to compute this density from the mass conservation equation. 2-Since CT scan images are the results of complex operations, we shall see in section §3 how to use matter density information to compute realistic CT scan images. The global principle of our approach is illustrated on Figure.1. The "numerical experiments" section exhibits a numerical validation.

WSCG 2006 conference proceedings, ISBN 80-86943-05-4
WSCG'2006, January 30 – February 3, 2006
Plzen, Czech Republic.

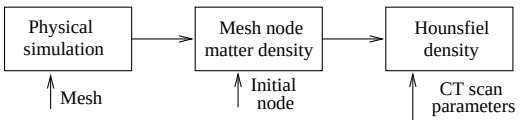

Figure 1: Illustration of the different steps of our work

2 STATE OF THE ART

CT scan device

CT scan devices aim at measuring electronic density of tissues by X-ray absorption. It is computed from the extraction of a set of attenuation coefficient μ defined for homogeneous materials by: $I = I_o.\exp^{-\mu x}$ where I is the intensity of the X-ray beam after crossing a thickness x of tissues

and I_o is the initial intensity of the x-ray beam (Cf Figure.2).

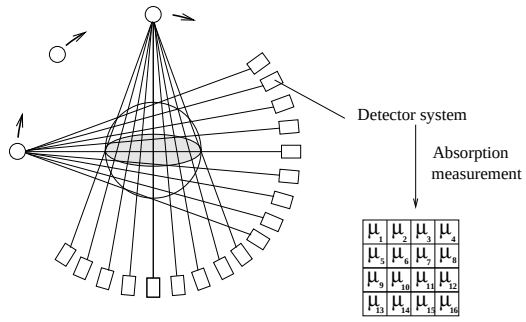

Figure 2: CT scan measurement principle

CT scan slices are reconstructed from a number of global attenuation coefficient measurements taken from various incidences. For each angle, the non absorbed beam dose hits then several detectors, producing 2D "density profiles" at several projection angles. To convert this set of 2D density profiles into attenuation coefficients, and then into 3D density, one has to "voxelize" the space. Each voxel is supposed to be homogeneous, isotropic and characterised by one attenuation coefficient. To constitute the voxels [G.T80] two successive operations are executed:

1. Retro-projection: it corresponds to a 3D reconstruction, i.e. the inverse projection of the numerical values obtained on the detector plane, to the 3D space coordinates [Rad17];

2. The Convolution or filtering: it consists in improving the quality of the reconstruction. We focus on this operation in the next section.

Convolution algorithm

The convolution algorithm (with filter or kernel) is defined by a mathematical process used to compensate the measurement errors related to the physics of the device (beam hardening, ...) and to the reconstruction operation. In the majority of CT-scan modules, several filtering algorithms are available. Aspect and characteristics of the resulting CT scan images depend strongly on the selected algorithm. According to clinical needs, it can be necessary to choose an algorithm that provides a higher space resolution, for the detailed representation of the bone and other volumes of high contrast such as pulmonary parenchyma. For example, algorithms developed for GE, Philipps, Siemens and Toshiba scanners are described in [Kea05]. Two kinds of deconvolution algorithms are commonly used: the bone kernel and the soft organs kernel. Bone kernel as presented in [SL74] allows sharp edges and accurate resolution, but is sensitive to noise. For the clinical applications where resolution is of less importance than contrast, for example, in lung CT scan, soft-organ kernels are used. The kernel described in [RL71] gives smooth edges, high contrast and is robust to noise. To summarise, image noise decreases with flattened convolution kernel, simultaneously reducing the space resolution and giving more details to low contrast zones (Cf Figure.3).

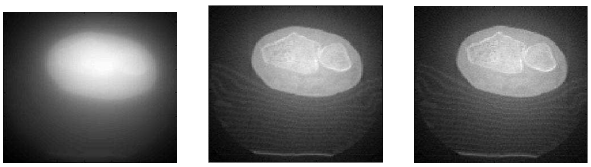

Figure 3: Filter influence: none (a.) soft tissue (b.) and bone (c.)

Scanner convolution modelling

In [JWS+03], the authors show how 3D CT scan data can be modelled as a linear system where an arbitrary cross section in a 3D image can be approximated by the following convolution: $g(x) = p(x) \otimes \lambda(x)$, where $p(x) = G_\sigma(x)$ is a 2D Gaussian function with σ as standard deviation, $g(x)$ is the selected cross section and $\lambda(x)$ is the real cross section, i.e., the true image. The optimal σ to produce the optimal image is found by statistical methods. Similar methods could be found in [WVS+98].

DRR image generation

Digitally Reconstructed Radiographs generation is a method to simulate CT scan slices. They are generated by ray-tracing techniques through a 3D volume extracted from CT scan but with a modified beam's eye view. The aim is to convert each voxel Hounsfield density into attenuation coefficient, x-ray energy specific. Several works describe DRR construction processes ([BDZ+99], [MBG+00]). Nevertheless, such techniques are only available when the geometry undergoes Euclidean transformations (rotations or translations) and cannot be applied to our case where solids are completely deformed, i.e. when the voxel density varies.

3 FORMALISATION

Our aim is to calculate the matter density in order to produce a 4D CT scan using the scanner convolution parameters associated to the clinical scanner devices. To do this, we assume that the density is a continuous function well represented by the interpolation functions of the mesh-points density values. We shall see that 4D CT scan can be built up from these density values.

Mesh node density computation

The only input we need are the displacement and the knowledge of the initial density (extracted from one CT scan) at each mesh node. In the following we denote $\mathbf{P}_j$ a mesh node, $\mathbf{U}$ a displacement and ρ_M the matter density. The key point of our approach is the mass conservation (Equation.1):

$$\frac{\partial \rho_M}{\partial t} + div(\rho_M.\mathbf{V}) = 0 \tag{1}$$

The interest of this equation, is the presence of the velocity $\mathbf{V}$ that could be replaced by displacement after integration. Let us then integrate Equation.1 over a small time step $[t_i, t_i + \Delta t]$: The *divergence* operator being independent of time, previous equation reads:

$$\rho(\mathbf{P}, t_i + \Delta t) - \rho(\mathbf{P}, t_i) + div \int_{t_i}^{t_i+\Delta t} (\rho.\mathbf{V})dt = 0 \tag{2}$$

Let $\Delta\rho = \rho(\mathbf{P}, t_i + \Delta t) - \rho(\mathbf{P}, t_i)$ be the required quantity. We note in Equation.2 the presence of ρ in $\int \rho.\mathbf{V}dt$ avoids a direct link with displacement. A Taylor series development of $\rho(p, ti - \Delta t)$ about t_i gives:

$$\begin{aligned} &\rho(\mathbf{P}, t_i - \Delta t) = \\ &\rho(\mathbf{P}, ti) + (\Delta t)\frac{\partial \rho(\mathbf{P}, t_i)}{\partial t} + O((\Delta t)^2) \end{aligned} \tag{3}$$

Finally due to the time integration Equation.2 reads :

$$\begin{aligned} &\Delta\rho = \\ &- div\left(\int_{t_i}^{t_i+\Delta t} \rho(\mathbf{P}, t_i).\mathbf{V}(\mathbf{P}, t)dt\right) + O((\Delta t)^2) \end{aligned} \tag{4}$$

$\rho(\mathbf{P}, t_i)$ is time independent then:

$$\Delta\rho \approx -div\left(\rho(\mathbf{P}, t_i).\int_{t_i}^{t_i+\Delta t} \mathbf{V}(\mathbf{P}, t)dt\right) \tag{5}$$

If we denote $\mathbf{U}_i(\mathbf{P})$ the displacement of the point $\mathbf{P}$ from the time t_i to the time $t_i + \Delta t$, velocity definition gives:

$$\Delta\rho \approx -div\left(\rho(\mathbf{P}, t_i).\mathbf{U}_i(\mathbf{P})\right) \tag{6}$$

One can now use the interpolation functions often considered in Finite Element Method [PFT+92]. In this method, the considered solid is subdivided into elements E_i composing a mesh. For any point $P \in E_i$ we have :

$$\begin{cases} \rho(\mathbf{P}, t_i) = \sum_{j \in E_i} N_j(\mathbf{P}).\rho(\mathbf{P}_j, t_i) \\ \mathbf{U}_i(\mathbf{P}) = \sum_{j' \in E_i} N_{j'}(\mathbf{P}).\mathbf{U}_i(\mathbf{P}_{j'}) \end{cases} \tag{7}$$

where $N_j(\mathbf{P})$ is the interpolation function at the node j. Then Equation.6 can be written for any point P in element E_i:

$$\Delta\rho \approx -\sum_{j,j'} \rho(\mathbf{P}_j, t_i).div\left(N_j(\mathbf{P}).N_{j'}(\mathbf{P}).\mathbf{U}_i(\mathbf{P}_{j'})\right) \tag{8}$$

Let us develop the *divergence* term considering now the space independence of $\mathbf{U}_i$:

$$\begin{aligned} &div(N_j(\mathbf{P}).N_{j'}(\mathbf{P}).\mathbf{U}_i(\mathbf{P})) = \\ &\frac{\partial N_j.N_{j'}}{\partial x}.U_x + \frac{\partial N_j.N_{j'}}{\partial y}.U_y + \frac{\partial N_j.N_{j'}}{\partial z}.U_z \end{aligned} \tag{9}$$

Finally for any $\mathbf{P}$, it is possible to calculate the divergence and then $\Delta\rho$ from the knowledge of:

- The node position $\mathbf{P}_j$;
- The node initial densities $\rho(\mathbf{P}_j, ti)$;
- The node displacements $\mathbf{U}_i(\mathbf{P}_{j'})$.

Scanner convolution

To compute the Hounsfield density of each voxel it could be possible to take only into account the contribution of each deformed element to the voxel, weighting this contribution by the percentage of voxel volume, within the deformed element volume (Cf Figure.4). Then it would be easy to transform the average density into Hounsfield density but the most tedious would be to evaluate the intersection volume. However it would not take into account the aspects of CT scan convolution process. Instead we propose to proceed to a convolution.

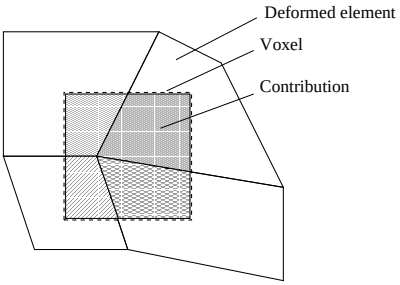

Figure 4: volume of deformed elements inside a considered voxel

The Hounsfield density $\rho_h(P)$ is an affine function of the matter density $\rho_M(P)$ [MBG+00]. Let $g(x) = ax + b$ be this function:

$$\rho_H(P) = a\rho_M(P) + b \tag{10}$$

From the previous section we get at each point the matter density $\rho_M(P)$. It is computed in any solid point by interpolation (Equation.7) of the node values $\rho_M(P_j)$ belonging to the mesh element E_i with the functions N_j :

$$\rho_M(P) = \sum_{j \in E_i} N_j(P)\rho_M(P_j) \tag{11}$$

By injecting (11) in (10) we obtain the Hounsfield density expression at any point P in an element E_i. Let us $\rho'_H(P')$ be the Hounsfield number at point P'. Its expression is given by a convolution of the mesh element density $\rho_H(P)$ with a kernel filter as the ones explained in the state of the art (Cf Figure.5).

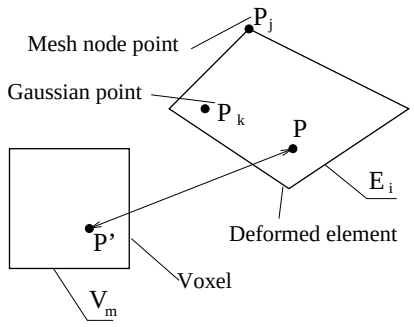

Figure 5: Mesh element influence on a voxel

$\rho'_H(P')$ is then given by:

$$\begin{aligned} \rho'_H &= f_\sigma \otimes \rho_H \\ &= f_\sigma \otimes (g \circ \rho_M) \end{aligned} \tag{12}$$

which reads:

$$\rho'_H(P') = \sum_{E_i} \int_{E_i} f_\sigma(\|P - P'\|^2).g(\rho_H(P))dP^3 \tag{13}$$

If one defines the densitometric value $D_H(V_m)$ at voxel V_m, as the average of the Hounsfield density function over the voxel, then the expression 13 has to be integrated over the voxel (Cf Figure.6). If we denote $\mathcal{V}_m$ the voxel volume:

$$D_H(V_m) = \frac{1}{\mathcal{V}_m} \int_{V_m} \rho'_H(P')dP'^3 \tag{14}$$

Injecting Equation.13 in Equation.14, we obtain:

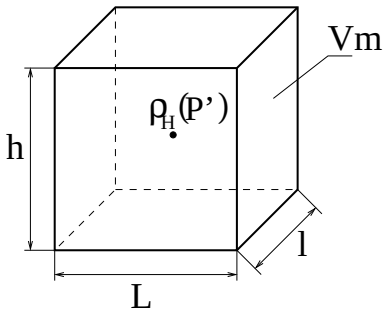

Figure 6: Voxel parameters

$$D_H(V_m) = \frac{a}{\mathcal{V}_m} \sum_{E_i} \int_{E_i} \rho_M(P) \int_{V_m} f_\sigma(\|P - P'\|^2)dP'^3.dP^3 + b \tag{15}$$

The latter simplification comes from the fact that the space integral of f_σ is equal to 1. The expression $I(P) = \int_{V_m} f_{sigma}(\|P - P'\|^2)dP'^3$ is independent of the function $\rho_h(P)$. Since the geometry of V_m is known and constant, an analytical expression for $I(P)$ can be derived. As it is often convenient we could consider for f_σ a truncated filter as presented in [THG00]. But the function must be integrated over the field given by the intersection of a voxel with a sphere.

This integration is tedious and a filter defined on an infinity space is thus used. We used the 3D Gaussian function with σ the standard deviation.

As previously seen , the $\rho_h(p)$ function can be expressed as a sum of interpolation functions of the node values, which gives to $D_H(V_m)$the expression:

$$\begin{aligned} &D_H(V_m) \\ &= \frac{a}{\mathcal{V}_m} \sum_{E_i} \sum_{j \in E_i} \int_{E_i} N_j(P)\rho_H(P_j)I(P)dP^3 + b \end{aligned} \tag{16}$$

The integral $\int_{E_i} N_j(P)\rho_H(P_j)I(P)dP^3$ can be integrated numerically by a Gaussian Quadrature [Gau94], which consists in a numerical estimations of an integral by picking optimal points called the Gaussian Points (P_k). Due to the element distortion, the integration domain is rather complex. It is then convenient to apply a reference change from a reference element of simple geometry to a real element. One has only to include the associated Jacobian matrix J:

$$\int_{E_i} N_j(P)\rho_H(P_j)I(P)dP^3 = \sum_{k\in E_i} w_k N_j(P_k)\rho_H(P_j).I(P_k)det_k \quad (17)$$

Where det_k represents the Jacobian determinant and w_k are weights associated with the Gaussian Points. Finally, the expression of the Hounsfield density on a voxel V_m of the scanner is given by the equation (18).

$$D_H(V_m) = \frac{a}{\mathcal{V}_m} \sum_{E_i} \sum_{j\in E_i} \sum_{k\in E_i} w_k N_j(P_k)\rho_H(P_j)I(P_k)det_k + b \quad (18)$$

4 RESULTS

This result step aims at validating our approach. Two computing phases are here qualitatively and quantitatively checked : matter density on mesh nodes and scanner convolution. The most critical stage is the node density computation because the mass conservation must be ensured. We shall test not only the mathematical validity but also the numerical validity.

Trial definition

The trial consists of pulling a cube fixed on one of its faces. Its edge length is 10 and the mesh is composed of small hexahedra with edge length $dx = dy = dz$ (Cf Figure.7).

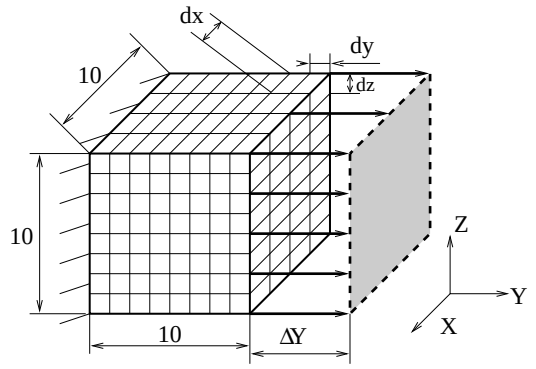

Figure 7: Trial cube geometry

The density in any point within the cube is set to 1 at initial state. The test consists in completely fixing one of the cube faces (plan **XZ** with $y = 0$) and in pulling the opposite face (plan **XZ** with $y = 10$) with a ΔY length in the direction of **Y** leaving free the **X** and **Z** displacements (Cf Figure.7). The cube stretching will be accompanied by a axial thinning in **X** and **Z**.

The interest of such kind of tests is the simplicity of this system in terms of mechanical behaviour. We can thus qualitatively evaluate if the calculations are realistic and self-consistent.

Figure 8 shows the displacements obtained by finite element method (FEM) computed with the software Code-Aster [Ast]. The displacements scale is voluntarily exaggerated to highlight the stretching in **Y** and the contraction in **X** and **Z**. The result is calculated with n computing steps.

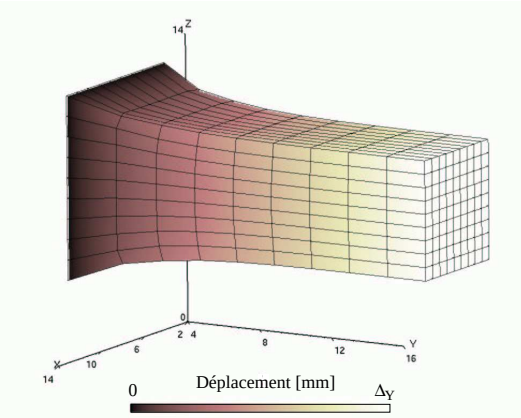

Figure 8: Displacements computed with FEM.The grey scale represents the displacement amplitude.

Numerical validation

The validation stages focus both on matter conservation and on CT scan imaging validations.

A first stage consists in a qualitative validation of the spatial evolution of the matter density . Figure 9 shows a continuous representation of density values computed on mesh nodes. It is a smoothing with the Gouraud method, i.e. colour interpolations. The transversal slice points out a density reduction in the centre of the cube due to pulling. As expected, in the periphery, as the volume decreases, the density increases. In between, the density remains close to 1. The longitudinal slice shows out a low density where the cube is fixed. Indeed at the vicinity of this zone, the volume increases. At the opposite face, free x and z displacements result in less shear and then less density changes.

All these observations are in full agreement with those that must be obtained. In other words we can conclude a qualitative validation. We can now study a more quantitative aspect by checking if the

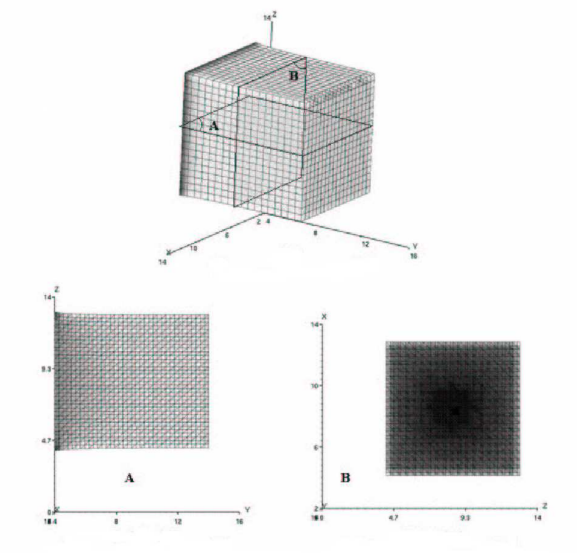

Figure 9: Continue representation of matter density. **A** : longitudinal slice. **B** : transversal slice.

system mass - i.e. the integral over the volume of the density - remains constant.

To evaluate the level of conformity we defined a mass loss error at each computing step:

$$Error[\%] = \frac{mass_{theorical} - mass_{computed}}{mass_{theorical}} \times 100 \quad (19)$$

which gives:

$$Error[\%] = \frac{m_0 - (\sum_{E_i} \int_{E_i} \rho_M^i(P)dP)}{m_0} \times 100 \quad (20)$$

where m_0 is the initial mass.

The results of these tests are gathered in the following Tables. The influence of several parameters on this error is shown. Table.1 deals with the number of computing steps n, which monitors the level of Taylor series approximation seen in (3). Table.2 deals with the applied-displacement amplitude, which fixes the level of distortion in geometry and Table.3 deals with mesh resolution and therefor with the accuracy of interpolating-function approximation.

The results of Tables 1, 2 and 3 show that the computing precision varies according to the computing number of steps (if it is multiplied by two, the error is approximately divided by two). The mesh resolution plays a less significant role, which

Computing step	*Total computing step number*			
	1	*5*	*10*	*100*
0.1n			0.008	0.001
0.2n		0.033	0.017	0.002
0.3n			0.025	0.004
0.4n		0.066	0.034	0.006
0.5n			0.043	0.008
0.6n		0.098	0.052	0.01
0.7n			0.061	0.013
0.8n		0.131	0.070	0.016
0.9n			0.079	0.02
n	0.796	0.163	0.089	0.0223

Table 1: n influence on mass conservation error with $\Delta Y = 10$ and $dx = 0.5$

Computing step	*Applied displacement*		
	1%	10%	100%
0.1n	0	0.008	0.796
0.2n	0	0.017	1.460
0.3n	0	0.025	2.052
0.4n	0	0.034	2.610
0.5n	0	0.043	3.162
0.6n	0.001	0.052	3.724
0.7n	0.001	0.061	4.312
0.8n	0.001	0.070	4.935
0.9n	0.001	0.079	5.602
n	0.001	0.089	6.322

Table 2: ΔY influence on mass conservation error with $dx = 0.5$ and $n = 10$

computing step	*Mesh resolution*		
	1	*0.5*	*0.25*
0.1n	0.008	0.008	0.008
0.2n	0.017	0.017	0.017
0.3n	0.025	0.025	0.025
0.4n	0.034	0.034	0.034
0.5n	0.043	0.043	0.042
0.6n	0.052	0.052	0.051
0.7n	0.061	0.061	0.060
0.8n	0.071	0.070	0.070
0.9n	0.081	0.079	0.079
n	0.091	0.089	0.089

Table 3: dx influence on mass conservation error with $\Delta Y = 10$ and $n = 10$

is a good point since on the other sides the computing time increases considerably with the number of elements. The last important observation is that a very significant displacement gives unacceptable errors. However this can be compensated by increasing the number of computing steps. We even conclude that a good criterion is to fix $\Delta Y/n$ small enough. For example, in the case of the 100% pulling (Cf Table.2), if calculation is carried out on

200 computation steps, the maximum error falls down to 0.461%.

The following test consists in checking if our defined convolution function is correct. To separate any possible errors in density calculation, we arbitrary fixed the density to 1 and show the result on Figure.10.

Figure 10: CT scan convolution with constant node density and $n = 10$. a) t=0, b) t=5, c) t=10

We observe a low grey level at the border due to the smoothing effect of the convolution. No artefact can be noted. The result given on Figure.11 includes the calculated density.

Figure 11: CT scan convolution with computed node density and $n = 10$. a) t=0, b) t=5, c) t=10

The results obtained are very satisfactory.

5 CONCLUSION

The method presented in this work converts mesh displacement into 4D CT scan. The apppealing aspect of our approach lies in the fact that the simulated-displacement data could be calculated with any kind of physical modelling resulting from 3D CT scan.

The module we built up needs only one parameter: the standard deviation σ of the CT scan device used for the signal treatment. Thus it remains the only data to obtain in order to have an effective 4D CT scan.

The success of our qualitative and quantitative validation now allow to go further: application of this module to a real organ motion and real density for clinical validation and finally a dynamic dosimetry.

REFERENCES

[Ast] Code Aster. *http://www.code-aster.org/*.

[BDZ+99] M.L Bahner, J. Debus, A. Zabel, S. Levegrun, and G. Van Kaick. Digitally reconstructed radiographs from abdominal CT scans as a new tool for radiotherapy planning. *Invest. Radiol.*, 34(7):643, 1999.

[Gau94] C.F. Gauss. Methodus nova integralium valores per approx. inveniendi. *Werke*, 3:163, 1794.

[G.T80] G.T.Herman. *Image Reconstruction from Projections*. Academic Press, New York, 1980.

[JWS+03] M. Jiang, C. Wang, M. Skinner, J. Rubinstein, and M. Vannier. Blind deblurring of spiral CT images. *IEEE Trans. Med. Imaging*, 22(7):837–845, 2003.

[Kea05] N. Keat. CT scanner automatic exposure control systems. Technical Report 05016, ImPACT, February 2005.

[MBG+00] N. Milickovic, D. Baltas, S. Giannouli, M. Lahanas, and N. Zamboglou. CT imaging based digitally reconstructed radiographs and their application in brachytherapy. *Physics in Medicine and Biology*, 45:2787–2800, 2000.

[PFT+92] W.H. Press, B.P. Flannery, S.A. Teukolsky, , and W. T. Vetterling. *Numerical Recipes in FORTRAN: The Art of Scientific Computing, 2nd ed.* Cambridge University Press, Cambridge, England, 1992.

[Rad17] J. Radon. Über die bestimmung von funktionen durch ihre integralwerte längs ge-wisser mannigfaltigkeiten. *Mathematisch-PhysikalischeKlasse*, 69(77), 1917.

[RL71] G.N. Ramachandran and A.V. Lakshminarayanan. Three dimensional reconstructions from radiographs and electron micrographs: Application of convolution instead of fourier transform. *Proc. Nat Acad Sci*, 68:2236–2240, 1971.

[SL74] L.A. Shepp and B.F. Logan. The fourrier reconstruction of a head section. *Trans. on Nuclear Science*, 21:21–43, 1974.

[THG00] T. Theußl, H. Hauser, and M.E. Gröller. Mastering windows: Improving reconstruction. Technical report, Institute of Computer Graphics and Algorithms, Austria, 2000.

[VBS+05] P-F. Villard, M. Beuve, B. Shariat, V. Baudet, and F. Jaillet. Simulation of lung behaviour with finite elements : Influence of biomechanical parameters. *IEEE, Mediviz, Conference on Information Visualization*, pages 9–14, 2005.

[WVS+98] G. Wang, M. W. Vannier, M. W. Skinner, M. G. P. Cavalcanti, and G. Harding. Spiral CT image deblurring for cochlear implantation. *Trans. Medical Imaging*, 17:251 – 262, 1998.